

# Indium doping induced defect structure evolution and photocatalytic activity of hydrothermally grown small SnO<sub>2</sub> nanoparticles

Raúl Sánchez Zeferino<sup>1</sup>, Umapada Pal<sup>\*2</sup>, Ma Eunice De Anda Reues<sup>2</sup> and Efraín Rubio Rosas<sup>3</sup>

<sup>1</sup> Departamento de Física, Universidad de Sonora, C.P. 8300, Hermosillo, Sonora, Mexico

<sup>2</sup> Instituto de Física, Universidad Autónoma de Puebla, Apdo. Postal J-48, Puebla, 72570 Mexico

<sup>3</sup> Centro Universitario de Vinculación y Transferencia de Tecnología, Benemérita Universidad Autónoma de Puebla, 24 sur y Av. San Claudio, Col. San Manuel, Puebla, Pue. 72570, Mexico

(Received July 7, 2018, Revised December 18, 2018, Accepted December 20, 2018)

**Abstract.** Well-crystalline SnO<sub>2</sub> nanoparticles of 4-5 nm size with different In contents were synthesized by hydrothermal process at relatively low temperature and characterized by transmission electron microscopy (TEM), microRaman spectroscopy and photoluminescence (PL) spectroscopy. Indium incorporation in SnO<sub>2</sub> lattice is seen to cause a lattice expansion, increasing the average size of the nanoparticles. The fundamental phonon vibration modes of SnO<sub>2</sub> lattice suffer a broadening, and surface modes associated to particle size shift gradually with the increase of In content. Incorporation of In drastically enhances the PL emission of SnO<sub>2</sub> nanoparticles associated to deep electronic defect levels. Although In incorporation reduces the band gap energy of SnO<sub>2</sub> crystallites only marginally, it affects drastically their dye degradation behaviors under UV illumination. While the UV degradation of methylene blue (MB) by undoped SnO<sub>2</sub> nanoparticles occurs through the production of intermediate byproducts such as azure A, azure B, and azure C, direct mineralization of MB takes place for In-doped SnO<sub>2</sub> nanoparticles.

**Keywords:** tin oxide nanoparticle; indium doping; defect structure; photocatalysis

## 1. Introduction

Among metal oxides, tin oxide (SnO<sub>2</sub>), an n-type semiconductor of wide direct band gap energy (3.65 eV at room temperature), attracted special attention due to its high optical transparency, and remarkable chemical and thermal stability. Recently, SnO<sub>2</sub> has been explored intensively for applications such as gas sensing (Li *et al.* 2002, Huang *et al.* 2005, Tadeev *et al.* 1999), dye-based solar cells (Shang *et al.* 2012), transparent conducting electrodes (Wager 2003), rechargeable lithium batteries (Han *et al.* 2005, Meduri *et al.* 2009), catalysts for oxidation and hydrogenation (Kansal *et al.* 2007, Carreno *et al.* 2004), and other optoelectronic devices (Wang *et al.* 2013, Tran *et al.* 2017). The performance of SnO<sub>2</sub> in these applications is much superior in nanostructure forms due to inherent characteristics of nanomaterials such as high surface area, tunable band gap energy, and agglomeration induced porosity, which are mainly derived from their smaller sizes. In fact, the optical, electrical, and optoelectronic properties of SnO<sub>2</sub> nanostructures can be tuned by controlling their size around the exciton Bohr radius (~2.7 nm) of the material (Shalan *et al.* 2016).

During the last two decades, a significant amount of effort has been devoted to fabricate SnO<sub>2</sub> nanostructures of different sizes and morphologies, utilizing co-precipitation (Bouaine *et al.* 2007) and other solution phase synthesis

(Gu *et al.* 2008) techniques. Physical growth techniques have also been utilized to fabricate SnO<sub>2</sub> nanostructures of different morphologies (García-Tecedor *et al.* 2016, Choi *et al.* 2008, Singh *et al.* 2012). However, hydrothermal has been the most widely used technique for fabricating SnO<sub>2</sub> nanostructures due to its convenient manipulation, combined with ability to control the size and morphology of the resulting nanostructures (Shi *et al.* 2013). High temperature and high pressure involved in hydrothermal process enhance the solubility of reactants, facilitating the involved chemical reactions (Wang and Rogach 2014).

Due to their small size, surface atoms of SnO<sub>2</sub> nanostructures play vital role on their physical and chemical properties. For example, Liu *et al.* (2011) have detected surface defects such as oxygen vacancies in SnO<sub>2</sub> nanocrystals responsible for the appearance of intense Raman band around 576 cm<sup>-1</sup> (Liu *et al.* 2011). On the other hand, impurification by metal ions drastically modifies the surface defects of SnO<sub>2</sub> nanoparticles, affecting not only their morphology, but also their electronic defect structures. While the incorporation of metal ions is known to affect the electronic and optical properties of SnO<sub>2</sub> nanostructures, which have been studied with great interest for their optoelectronic applications, incorporated metal ions are also expected to affect the normal catalytic and photocatalytic performances of SnO<sub>2</sub> nanoparticles. In fact, several metals such as Zn, Cu, Ag, Ni, V, and Cr have been utilized to dope SnO<sub>2</sub> nano- and microstructures to evaluate their photocatalytic performances under UV and visible irradiations (Shanmugam *et al.* 2016, Babu *et al.* 2017, Vignesh *et al.* 2013, Chen *et al.* 2015, Reddy *et al.* 2016).

\*Corresponding author, Ph.D., Professor,  
E-mail: [upal@ifuap.buap.mx](mailto:upal@ifuap.buap.mx)

In the present work, we investigate the effect of In doping on size, crystallinity, optical and photocatalytic behavior of small SnO<sub>2</sub> nanoparticles grown by hydrothermal process. Evolution of defect structure in the SnO<sub>2</sub> nanoparticles due to In incorporation has been studied by Raman and photoluminescence spectroscopy along with high-resolution transmission electron microscopy. Performance of the nanostructures in photocatalytic degradation of organic dyes under ultra-violet (UV) irradiation has been studied over a standard test dye methylene blue (MB). Probable mechanism of dye degradation by SnO<sub>2</sub> nanoparticles and the effect of incorporated In in the nanostructures have been discussed.

## 2. Experimental

SnO<sub>2</sub> nanoparticles of ~5 nm average size were synthesized by hydrothermal method, following the procedure we reported earlier (Sánchez Zeferino *et al.* 2013), with some modification. Briefly, the solutions of SnCl<sub>4</sub>·5H<sub>2</sub>O (0.5 M) and NaOH (1.0 M) in deionized water were prepared independently. The NaOH solution was added slowly to tin chloride solution under magnetic stirring until the pH of the mixture reaches 9. After 30 min of agitation, the pH of the mixtures was readjusted, and different amounts of In(NO<sub>3</sub>)<sub>3</sub>·xH<sub>2</sub>O (2.0, 8.0 and 16.0 mol % nominal) were added into it under magnetic stirring. The resulting white solution was then transferred to a Teflon autoclave and heated at 180°C for 24 h. After cooling down to room temperature, the white precipitate was separated by centrifugation and washed several times with ethanol and water. Finally, the obtained product was dried in air at 70°C for 2 h.

The morphology of the undoped and In-doped nanoparticles was analyzed in a Philips Tecnai F30 high resolution transmission electron microscope (HRTEM) operating under 300 KeV accelerating voltage. X-ray diffraction (XRD) patterns of the samples were recorded in a Bruker AXS D8 Discover diffractometer using monochromatic CuK radiation ( $\lambda = 1.5406\text{\AA}$ ). Energy dispersive spectroscopy (EDS) attached to a JEOL JSM-7800F field-emission scanning electron microscope with attached Oxford Instrument X-Max spectrometer was utilized to analyze the elemental composition of the nanostructures. Raman spectra of the samples were recorded in the 200-700 cm<sup>-1</sup> spectral range using a Horiba, JOBIN-YVON microRaman spectrometer with 633 nm line of He-Ne laser as excitation source. The UV-Vis diffuse reflectance spectra of the samples were acquired in the 200-800 nm spectral range on a Varian UV-Vis-NIR Carry 100 spectrophotometer, equipped with an integrated sphere (DRA-CA-30I). Photoluminescence (PL) spectra of the doped and undoped nanostructures were recorded at room temperature (293K) exciting them by 325 nm line of a He-Cd laser under vacuum.

The photocatalytic activity of the undoped and In-doped SnO<sub>2</sub> nanoparticles was studied in a cylindrical glass reactor of 250 ml capacity (50 mm internal diameter and 120 mm height) fitted with water recirculating jacket. Typically, 40

mg of the sample was added into 80 ml of methylene blue (MB) dye solution (10 ppm) under magnetic stirring and air bubbling in dark (inside a black box). The temperature of the reaction mixture was maintained at 20°C throughout the experiment, utilizing the water recirculating jacket. The mixture was left in dark for 90 min to reach the adsorption-desorption equilibrium at the surface of the catalyst. The extent of dye adsorption was determined from the decrease of MB concentration in the solution by monitoring the intensity of its principal absorption bands (500-750 nm) in a Shimadzu UV-VIS-NIR 3100PC spectrophotometer. At different intervals of time, about 4 ml of aliquot was withdrawn from of the mixture and filtered by a reusable syringe (z268410) fitted with a nitrocellulose membrane filter of 0.22 mm pore size, to measure the dye concentration in the filtered solution. To determine the dye concentration in the aliquots, a pre-calibrated absorption curve of MB solution was utilized. Once the dye adsorption-desorption equilibrium is reached, the mixture was illuminated by a 365 nm emission diode array of 10 W. The concentration of MB in the mixture was monitored through the same way as in the case of dye adsorption under dark.

## 3. Results and discussion

Fig. 1 shows typical TEM images of the SnO<sub>2</sub> nanostructures prepared with different nominal indium contents. All the samples revealed the formation of well-dispersed small quasi-spherical particles during hydrothermal process. The morphology of the nanostructures does not change significantly with the increase of nominal In content in the reaction mixture. HRTEM images of the undoped and In-doped SnO<sub>2</sub> nanoparticles presented in Fig. 1 revealed predominant (110) and (101) planes of tetragonal SnO<sub>2</sub> lattice with interplanar spacing of 0.33 and 0.26 nm, respectively. A slight increase of interplanar spacing in some of the particles can be noticed for the samples with high indium contents (nominal 8.0 and 16.0 mol %). The HRTEM images the nanostructures indicate their high crystallinity, as the particles contain single crystalline grains. The average size of the undoped and doped nanoparticles was estimated from their size distribution histograms (Fig. 1, right panel). To construct the size distribution histograms, the size of individual particles was estimated by measuring their dimensions from TEM images. Estimated average particle size varied from  $4.2 \pm 0.6$  nm for undoped sample to  $5.2 \pm 0.8$  nm for the sample doped with nominal 16.0 mol % In, clearly indicating a lattice expansion due to In doping.

The crystallinity and structural phase of each of the samples were examined further by X-ray diffraction (XRD). The XRD patterns of the nanostructures presented in Fig. 2 revealed clear diffraction peaks correspond to the (110), (101), (200), (211), (220), (002), (310), (112), (202), (321), and (222) planes of SnO<sub>2</sub> in tetragonal phase (JCPDS Card No: 41-1445). There appeared no diffraction peak associated to indium, indium oxide, or any other impurity phase in the samples. As can be seen in Fig. 2, the intensity

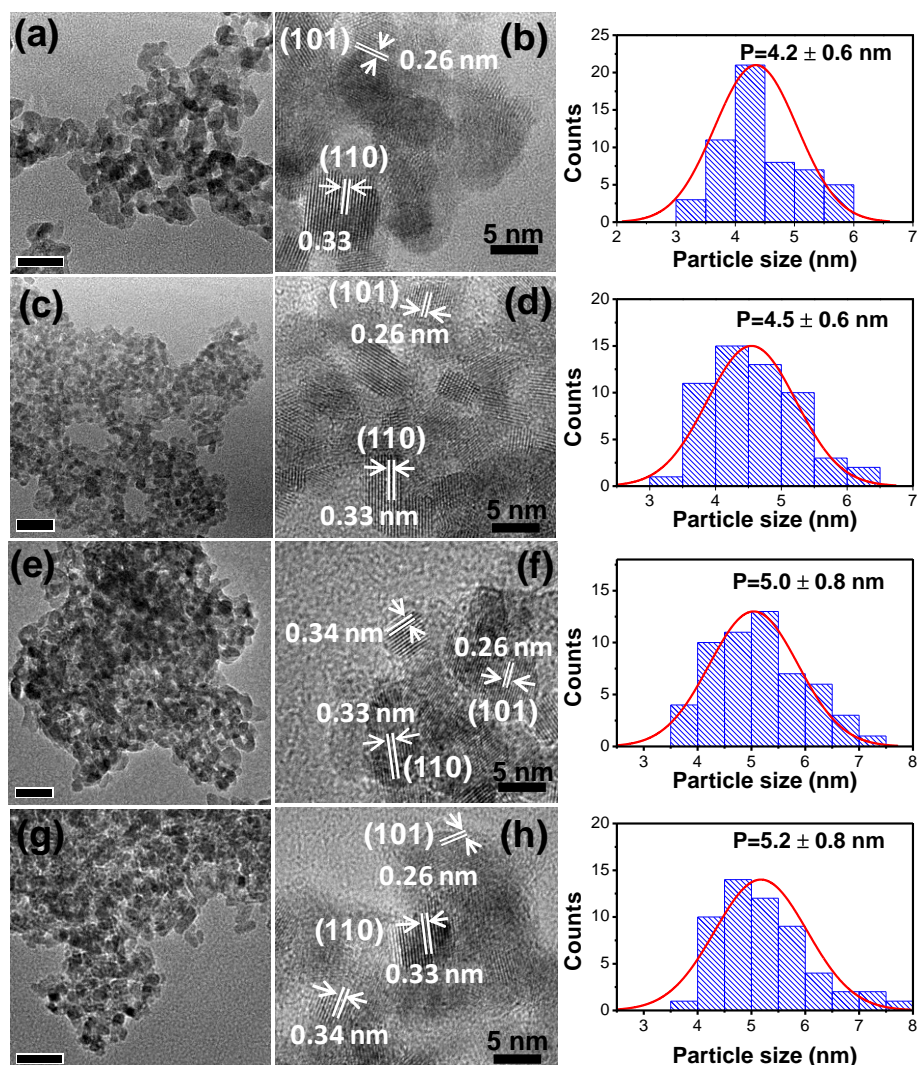


Fig. 1 Typical TEM and HRTEM images of SnO<sub>2</sub> nanoparticles prepared with (a-b) 0.0 %, (c-d) 2.0 %, (e-f) 8.0 %, and (g-h) 16.0 % nominal In. Corresponding size distribution histograms are shown in the right side panel

of the main diffraction peaks located at 26.5, 33.8, and 51.6 increased with the increase of In content in the nanostructures with no significant shift in their positions, indicating an enhanced crystallinity or increase in grain size due to In incorporation. Average grain size and lattice strain in the nanoparticles were calculated using the Williamson-Hall equation

$$\beta \cos \theta = \frac{0.9\lambda}{D} + 4\varepsilon \sin \theta \quad (1)$$

where D is effective crystallite size,  $\varepsilon$  is the lattice strain,  $\beta$  is the full width at half maximum (FWHM) of the selected diffraction peak in radians,  $\lambda$  the wavelength of X-ray, and  $\theta$  the diffraction angle. In Fig. 2(b), the  $\beta \cos \theta / 0.9\lambda$  ratios were plotted against  $4 \sin \theta$  for the prominent diffraction peaks, and the average crystallite size and lattice strain in the samples were estimated from the y-axis intercept and slope of the corresponding linear fits. The average crystallite size (D) and lattice strain ( $\varepsilon$ ) estimated for the undoped and In-doped SnO<sub>2</sub> nanoparticles are presented in Table 1. As can be seen in Table 1, the values of lattice strain ( $\varepsilon$ ) and

crystallite size (D) increased from 2.23 to 2.28 % and 2.6 to 2.7 nm, respectively, with the increase of In content in the nanostructures.

The lattice parameters ( $a$  and  $c$ ) of the tetragonal nanostructures were calculated using the formula

$$\frac{1}{d_{hkl}^2} = \frac{h^2 + k^2}{a^2} + \frac{l^2}{c^2} \quad (2)$$

where  $d_{hkl}$  is the interplanar spacing between planes, and  $h, k, l$  are the Miller indices. As can be seen in Table 1, the estimated lattice parameter values are close to their expected values, with marginal increase due to In incorporation, probably due to a mild deformation of SnO<sub>2</sub> lattice (Higler and Sprake 2017).

The EDS spectra of the nanostructures revealed the presence of O, Sn and O, Sn, In in the undoped and In-doped nanostructures, respectively, without any other element. From the EDS estimated elemental composition presented in Table 2, we can see the indium contents in the doped samples are far below than their nominal values. The maximum In content in the nanostructures of highest

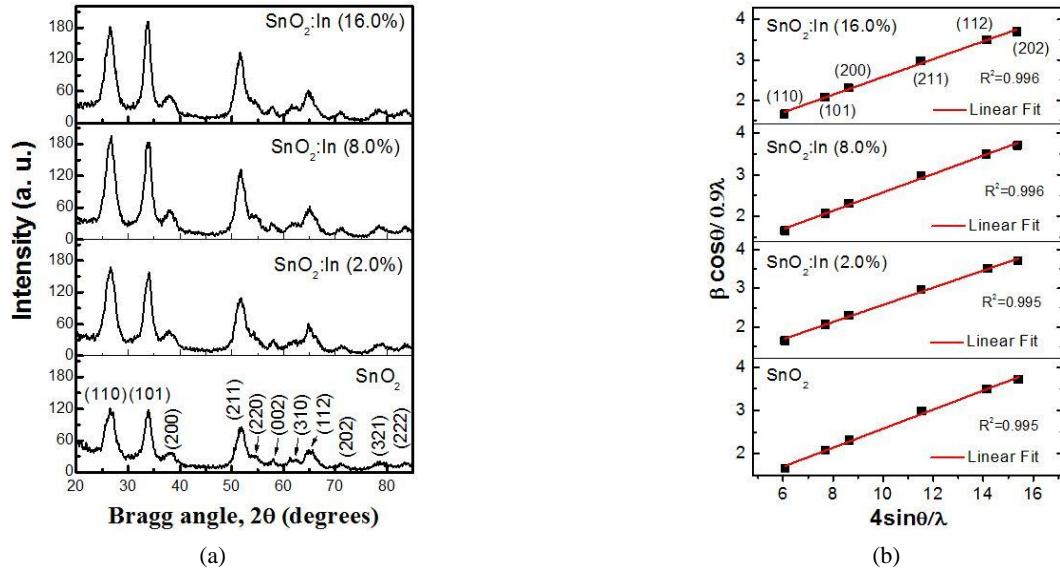


Fig. 2 (a) XRD patterns; and (b)  $\beta\cos\theta/0.9\lambda$  vs  $4\sin\theta/\lambda$  plots for the undoped and In-doped  $\text{SnO}_2$  nanoparticles

Table 1 Average crystallite size (D), particle size (P), lattice strain, and lattice parameters of the fabricated undoped and In-doped  $\text{SnO}_2$  nanoparticles

Indium [nominal %]	Average crystallite size [nm]	Particle size from TEM [nm]	Lattice strain $\epsilon$ [%]	Lattice parameters		$c/a$ ratio
				$a$ [Å]	$c$ [Å]	
0	2.6	$4.2 \pm 0.6$	2.23	4.743	3.194	0.6734
2.0	2.6	$4.5 \pm 0.6$	2.23	4.745	3.191	0.6725
8.0	2.7	$5.0 \pm 0.8$	2.25	4.743	3.194	0.6735
16.0	2.7	$5.2 \pm 0.8$	2.28	4.754	3.203	0.6739

Table 2 Chemical composition (atomic %) of the In-doped  $\text{SnO}_2$  nanoparticles obtained from EDS results

Sample	O [at.%]	Sn [at.%]	In [at.%]
$\text{SnO}_2$	70.14	29.86	--
$\text{SnO}_2:\text{In}$ (2.0%)	70.72	29.29	0.02
$\text{SnO}_2:\text{In}$ (8.0%)	70.01	29.55	0.44
$\text{SnO}_2:\text{In}$ (16.0%)	69.69	28.76	1.56

nominal In content (16%) is only around 1.56 atom %. The low indium content in the samples explains why the lattice strain and lattice parameters ( $a$  and  $c$ ) of the In-doped nanostructures do not differ significantly from the values of undoped nanostructures. The EDS estimated atomic ratio of Sn and O in all the samples remained higher than 1:2, indicating an oxygen excess and/or tin deficiency at the surface of the nanoparticles.

Fig. 3 shows the room temperature Raman spectra of undoped and In-doped  $\text{SnO}_2$  nanoparticles. All the samples revealed a broad, intense dispersion band spanning over 400 to 700  $\text{cm}^{-1}$  with several humps along with two weaker bands near 355 and 775  $\text{cm}^{-1}$ . A computer-assisted deconvolution of the broad band revealed four components around 470, 545, 580, and 635  $\text{cm}^{-1}$ . The bands appeared around 470, 635 and 775  $\text{cm}^{-1}$  correspond to the common  $E_g$ ,  $A_{1g}$  and  $B_{2g}$  Raman active modes of crystalline  $\text{SnO}_2$  in

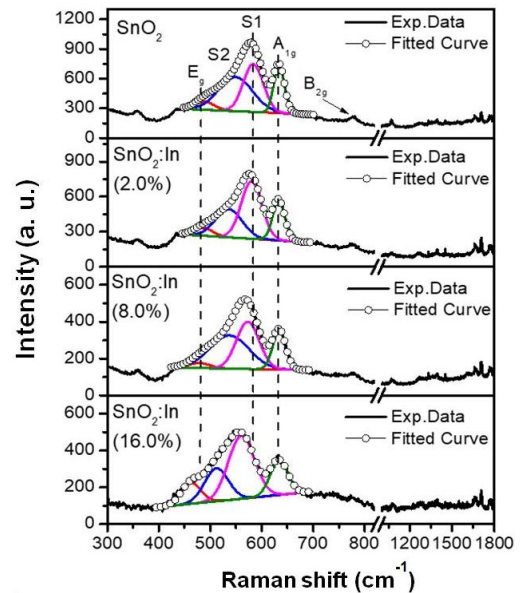


Fig. 3 Raman spectra of the undoped and In-doped  $\text{SnO}_2$  nanoparticles

tetragonal phase (Reddy *et al.* 2017). While  $A_{1g}$  and  $B_{2g}$  are two non-degenerate modes associated to the vibration of oxygen atoms in the plane perpendicular to  $c$  axis, the doubly degenerate  $E_g$  mode vibrates along the  $c$  axis

(Diéguez *et al.* 2001). The band revealed around 355  $\text{cm}^{-1}$  has been frequently assigned to the surface mode of  $\text{SnO}_2$  nanostructures (Zuo *et al.* 1994). In fact, appearance of surface modes in the Raman spectra of nanometric  $\text{SnO}_2$  has been reported to appear mainly in three regions (Diéguez *et al.* 2001): in the 576-568  $\text{cm}^{-1}$  (S1), 542-486  $\text{cm}^{-1}$  (S2), and 691-707  $\text{cm}^{-1}$  (S3) spectral ranges. The positions of both the S1 and S2 modes are seen to shift towards lower energy along with a reduction in intensity on the increase of particle size (Diéguez *et al.* 2001). As can be seen in Fig. 3, the S1 band appeared around 582  $\text{cm}^{-1}$  for the undoped nanostructures, and shifted gradually towards lower wavenumber with the increase of In content (Table 3). As can be noticed from Table 3, although the incorporation of In in  $\text{SnO}_2$  nanoparticles affects the position of the S1 surface mode, the position of the  $A_{1g}$  classical mode remains almost unchanged (around 635  $\text{cm}^{-1}$ ) for all the samples. However, the  $A_{1g}$  mode becomes broader with the increase of In content in the nanoparticles (Table 4). The broadening of the classical  $A_{1g}$  mode can be ascribed to oxygen deficiency (Diéguez *et al.* 2001) and crystal distortion due to indium ion incorporation into  $\text{SnO}_2$  structure. Similar structural modifications have been observed by Ji *et al.* (2006) for their In-doped  $\text{SnO}_2$  thin films. Additionally, the broadening of  $A_{1g}$  mode has been also predicted due to a reduction of particle/grain size of  $\text{SnO}_2$  nanostructures (Diéguez *et al.* 2001). However, the variation of average size of the nanostructures fabricated in this work is small (5.2 to 4.2 nm, see Fig. 1). Therefore, the broadening of  $A_{1g}$  mode in In-doped  $\text{SnO}_2$  nanoparticles probably due to their structural defects such as oxygen vacancies, tin interstitials or the formation of an amorphous

shell around the crystalline particles (Diéguez *et al.* 2001). Such assumption is also supported by the observed shift of the  $E_g$  mode (Table 3), which suffers even bigger shifts towards higher frequency with the variation of particle size. As can be seen, the position of the  $E_g$  mode shifts towards lower frequency with the increase of In content in the nanostructures. On the other hand, several weak dispersion peaks appeared in the 900 to 1800  $\text{cm}^{-1}$  spectral range for all the samples.

While the Raman bands appeared around 1070, 1445, and 1770  $\text{cm}^{-1}$  have been associated to the formation of metal carbonate due to reactive adsorption of ambient  $\text{CO}_2$  over the metal oxide nanostructures (Busca and Lorenzelli 1982), the bands appeared around 1660 and 1706  $\text{cm}^{-1}$  have been attributed to carbonyl (C = O) groups (Horvath *et al.* 2005). Utilization of NaOH solution for the adjustment of solution pH during the synthesis of  $\text{SnO}_2$  nanoparticles in the present study might have favored the reactive adsorption of  $\text{CO}_2$  at the surface of the nanostructures and formation of carbonate compound.

Fig. 4(a) presents the diffuse reflectance spectra (DRS) of the fabricated  $\text{SnO}_2$  nanoparticles. All the samples revealed characteristic absorption edge near 340 nm. While both the undoped and In-doped samples revealed their high reflectance (60-70%) in the visible spectral range, the reflectance of In-doped  $\text{SnO}_2$  samples decreased slightly with the increase in indium content. The diffuse reflectance spectra of the samples were plotted after Kubelka-Munk (K-M) treatment (Escobedo Morales *et al.* 2007) to estimate their band gap ( $E_g$ ) energy (Fig. 4(b)). The estimated  $E_g$  values of the samples varied from 4.2 to 4.1 eV with the increase of In content. The higher band gap energy of the nanoparticles than the same of bulk  $\text{SnO}_2$  (~3.65 eV) can be attributed to the quantum confinement effect as the average diameter of all the nanoparticles are smaller than the exciton Bohr diameter of  $\text{SnO}_2$  (~5.4 nm).

To verify the quantum confinement effect in the fabricated nanoparticles, the band gap energy of the semiconductor as a function of the particle size was calculated using the Brus equation (Yanes *et al.* 2010)

$$E_g(R) \approx E_g^{Bulk} + \frac{\hbar^2 \pi^2}{2R^2} \left( \frac{1}{m_e^*} + \frac{1}{m_h^*} \right) \quad (3)$$

where  $E_g(R)$  is the band gap energy of nanoparticles, R is

Table 3 Position and FWHM of classical  $A_{1g}$ ,  $E_g$  modes and S1 surface vibrational mode of  $\text{SnO}_2$  nanoparticles containing different In contents

Sample	Position of vibrational modes [ $\text{cm}^{-1}$ ]		
	$A_{1g}$ (FWHM)	S1 (FWHM)	$E_g$ (FWHM)
$\text{SnO}_2$	635 (23)	582 (46)	489 (52)
$\text{SnO}_2:\text{In}$ (2.0 %)	635 (26)	580 (47)	486 (43)
$\text{SnO}_2:\text{In}$ (8.0 %)	635 (28)	572 (54)	479 (49)
$\text{SnO}_2:\text{In}$ (16.0 %)	636 (36)	560 (59)	468 (35)

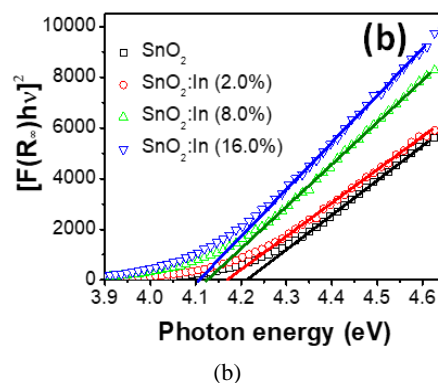
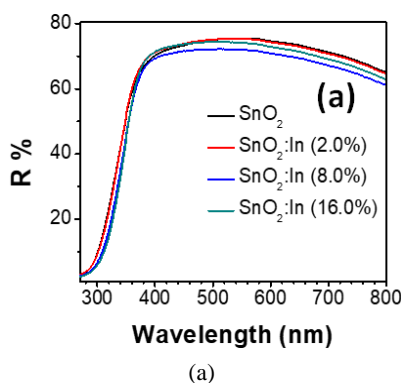


Fig. 4 (a) DRS spectra; and (b) K-M plots of the diffuse reflectance spectra of undoped In-doped  $\text{SnO}_2$  nanoparticles

the nanoparticle radius,  $E_g^{Bulk}$  is the band gap of the bulk semiconductor and  $m_e^*$  and  $m_h^*$  are the effective mass of electrons and holes, respectively. For the calculation of  $E_g(R)$  of In-doped SnO<sub>2</sub> nanoparticles, we will assumed  $E_g^{Bulk} = 3.65$  eV,  $m_e^* = 0.27m_e$ , and  $m_h^* \gg m_e^*$ .

As can be noticed in Fig. 5, while the Brus model predicts a drastic increase in band gap energy for SnO<sub>2</sub> particles smaller than 5 nm, the variation is relatively small for the particles of 5-10 nm size range. The band gap energies of the SnO<sub>2</sub> nanoparticles fabricated in the present study have been plotted in Fig. 5 against their TEM estimated average diameters. We can see a difference of about 0.3 eV between the DRS estimated band gap energy and the Brus model estimated band gap energy values. While such a difference (almost constant) in band gap energy (towards higher energy) can be due to the polycrystalline nature of the fabricated nanoparticles with average grain size considerably smaller than average

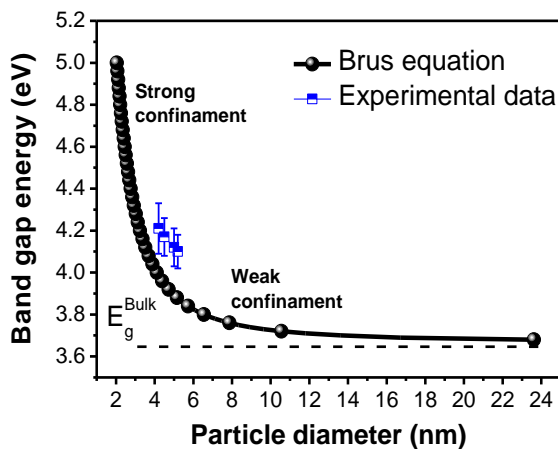


Fig. 5 A comparison between the band gap energy of SnO<sub>2</sub> nanoparticles estimated from their DRS spectra and calculated using Brus relation

particle size (see Table 1), contribution of In incorporation on the variation of band gap energy cannot be ruled out. While an increase of effective band gap energy due to incorporation of indium in small atom % due to the filling of vacant electronic states at the conduction band of SnO<sub>2</sub> is quite unexpected as indium in SnO<sub>2</sub> acts as an acceptor impurity, a reduction in density of donor state levels below the conduction band due to indium doping is very much expected. To verify the effect, we measured the electrical resistivity of the nanostructures on their cold pressed pellets (~6.0 mm diameter and ~2 mm thickness) using colloidal graphite paste (aguadag, TED Pella, Inc.) as contacts, observing only a nominal decrease in resistivity due to In-doping. For example, while the resistivity of the undoped sample was 253.0  $\Omega$ .m, the resistivity of the nanostructures with highest indium content (16% nominal) was about 223.0  $\Omega$ .m. Such a small decrease in resistivity of the nanostructures might be due to the formation of oxygen vacancies due to indium incorporation (Teresa 2017).

PL study was performed further to study the effect of indium doping on the defect structure of the nanostructures. Room temperature PL spectra of the undoped and In-doped SnO<sub>2</sub> nanoparticles are shown in Fig. 6. As can be seen, the PL spectra of both the undoped and In-doped SnO<sub>2</sub> nanoparticles exhibit an intense broad emission band in 400-750 nm range, centered around 530 nm (2.3 eV). A computer assisted Gaussian deconvolution of this emission band revealed two components: a green component (519-525 nm) and a yellow component (570-582 nm). According to literature, both of these emission bands are associated to crystalline defects such as oxygen vacancies, Sn vacancies or Sn interstitials, which form a considerable number of trapped states within the band gap of SnO<sub>2</sub> nanostructures (Xiang *et al.* 2008). In fact, both the green and yellow emissions in SnO<sub>2</sub> have been attributed to oxygen vacancies (Peché-Herrero *et al.* 2014, Zhou *et al.* 2011). As can be seen from the Raman spectra (Fig. 3) of the fabricated nanoparticles, some of the fundamental and surface

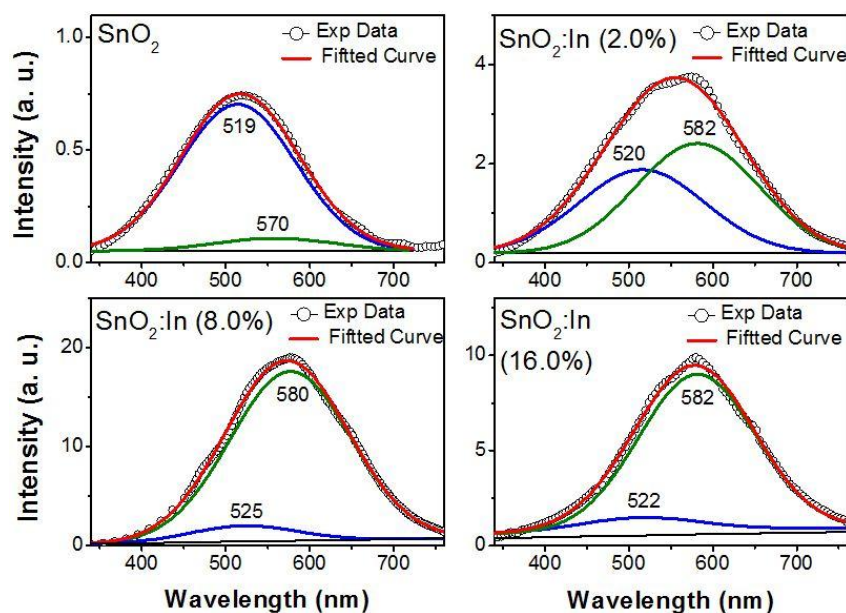


Fig. 6 Room temperature PL spectra of the undoped and In-doped SnO<sub>2</sub> nanoparticles

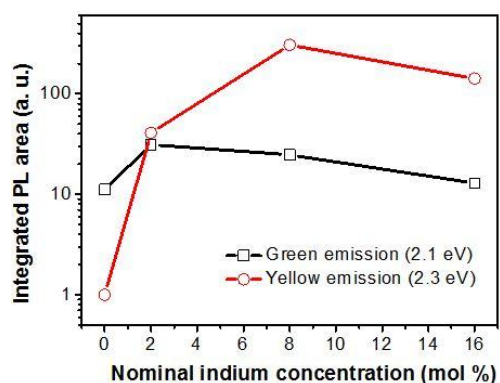


Fig. 7 Effect of indium concentration on integrated PL intensity of In-doped SnO<sub>2</sub> nanoparticles

vibrational modes suffer positional shift and widening on In incorporation, due to the formation of surface defects. While oxygen vacancies are the most frequent surface defect in metal oxide nanostructures, in the present case, surface oxygen vacancies can be classified into two types: oxygen bringing vacancies coordinated with neighboring Sn, forming an angle of 100° on the surface of the (110) and (100) planes of a SnO<sub>2</sub> structure, and in-plane oxygen vacancies forming an angle of 130° in the (110), (101), and (001) planes (Jean and Her 2009). While the green emission (~2.3 eV) has been associated to the surface oxygen vacancies of 100° coordinated, the yellow emission (~2.1 eV) has been correlated to 130° coordinated oxygen vacancies (Cheng *et al.* 2010). While the undoped SnO<sub>2</sub> nanoparticles exhibit both of these green (~2.3 eV) and yellow (~2.1 eV) emissions with no significant alteration in their positions, the emissions are significantly strong for the In-doped nanoparticles (Fig. 6). To understand such redistribution of defect structures in the nanoparticles, the integral intensities of the two component emissions (green and yellow) were plotted against nominal In concentration (Fig. 7). As can be noticed in Fig. 7, the intensity of both the green and yellow emissions increase more than two orders with In incorporation. While the intensity of green emission is maximum for a nominal 2 mol % In doping, the intensity of the yellow emission grows until a nominal 8 mol % of In. However, the intensity of both the emissions decreases for higher In % (beyond 8 mol %). The increase of green and yellow emissions in In-doped SnO<sub>2</sub> nanoparticles can be explained on the basis of In ions incorporation into the SnO<sub>2</sub> matrix. As the ionic radius of In<sup>3+</sup> (0.80 Å) is only about 11.6 % higher than the ionic radius of Sn<sup>4+</sup> (0.69 Å), some of the In<sup>3+</sup> ions substitute Sn<sup>4+</sup> ions in the host lattice (Sun *et al.* 2014), creating electron deficiency. The deficiency of one electron or creation of a hole can be considered as an oxygen vacancy. In fact, the observed intensity increase of the green and yellow emission bands in the nanoparticles with increasing doping concentration is due to the formation of oxygen vacancies, which was also noted in the Raman spectra of the In-doped nanoparticles. However, the intensity of the visible luminescence emissions (2.1 and 2.3 eV) decreases for higher indium concentrations (e.g. for the sample SnO<sub>2</sub>:In (16.0 %)). Such a reduction of visible emissions in the

nanoparticles containing very high In contents can be understood considering the solubility of indium in SnO<sub>2</sub> lattice. Due to the difference in ionic radii, the substitution of Sn<sup>4+</sup> ion by In<sup>3+</sup> is partial. Hence, some of the incorporated indium ions would segregate to grain boundaries. As the fabricated nanoparticles are of high crystalline quality, mostly containing single grain structures, the segregated In<sup>3+</sup> ions would create electron capture centers at the surface of nanoparticles, generating nonradiative decay channels (Guan *et al.* 2014). Formation of such electron capture centers at the surface due to high dopant concentration and consequent reduction of visible emission have also been noticed for SnO<sub>2</sub> nanostructures with high concentration of dopants such as Eu (Kou *et al.* 2016) and Al (Li *et al.* 2017).

Incorporation of In in SnO<sub>2</sub> nanoparticles also induces a structural disorder of SnO<sub>2</sub> lattice, which can be seen in the broadening of the fundamental mode A<sub>1g</sub> in the Raman spectra of the In-doped samples. Moreover, the surface mode S1 suffers a significant shift (~22 cm<sup>-1</sup>) with increasing indium concentration. All the visible emissions in SnO<sub>2</sub> nanoparticles are attributed mainly to defects associated to oxygen vacancies.

Among all the factors such as composition, structural phase, particles size, defect structures, surface hydroxyl groups, etc. that influence the photocatalytic activity of metal oxide semiconductors (Anuchai *et al.* 2018, Zhang *et al.* 2014), the surface oxygen vacancies are very important in the process of photocatalysis because they modify the electronic structure of the semiconductor.

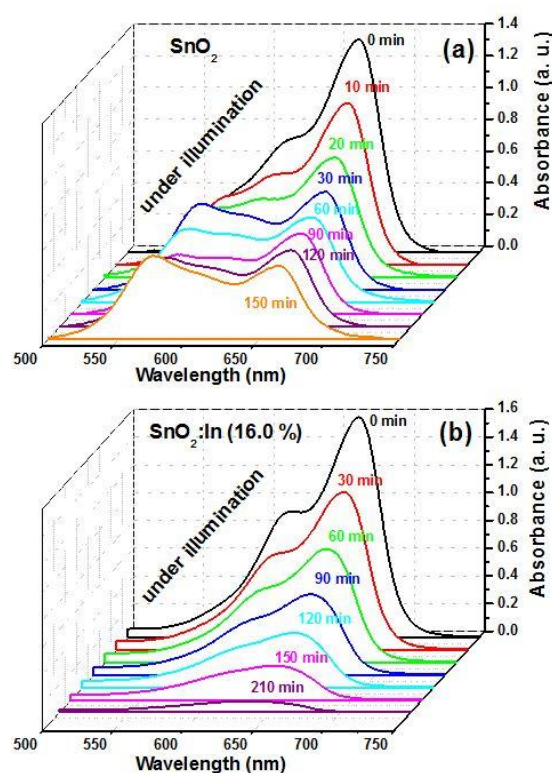


Fig. 8 Temporal evolution of MB absorption spectra for the undoped and In-doped (16.0% nominal) SnO<sub>2</sub> nanoparticles under UV illumination

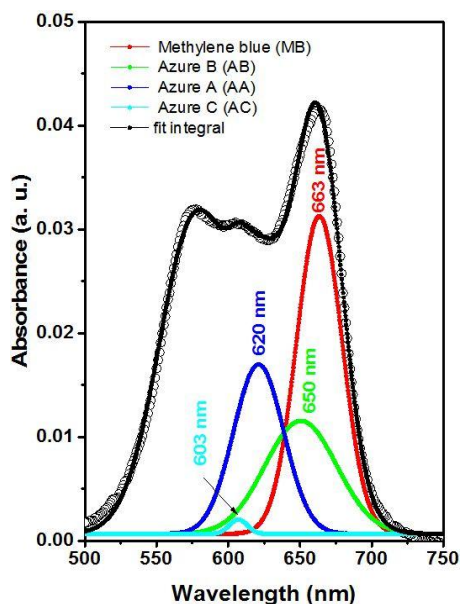


Fig. 9 Absorption spectra of methylene blue (MB) after 90 minutes of UV illumination in presence of undoped  $\text{SnO}_2$  nanoparticles utilized to deconvolute the component bands. The component bands associated to different intermediates produced by photocatalytic degradation are shown in green, blue and sky-blue colors. Open circles correspond to the original spectrum, and black line corresponds to fit integral

To test the photocatalytic performance of the fabricated  $\text{SnO}_2$  nanoparticles and the effect of In incorporation in them, undoped and In-doped samples were tested for MB degradation under UV light. The absorption spectra of MB revealed most intense absorption peak at 663 nm with a shoulder around 612 nm, which correspond to MB monomer and MB dimer  $[(\text{MB})_2]$ , respectively (Fig. 8) (Flores *et al.* 2014). During photocatalytic degradation, while the intensity of both the absorption bands diminished gradually, the absorption spectra of the undoped sample revealed several new bands (Fig. 8(a)), indicating the generation of intermediate products during photocatalytic

degradation of MB. A computer assisted deconvolution of the absorption spectra (Fig. 9) revealed three component (apart from the MB monomer) bands which correspond to intermediate byproducts of MB degradation such as azure B (AB), azure A (AA) and azure C (AC), with peak positions around 650, 620 and 603 nm, respectively (Zhang *et al.* 2001). It is worth mentioning that the absorption spectra correspond to all the In-doped  $\text{SnO}_2$  catalysts revealed similar behavior (Fig. 8(b)). In contrary to the undoped catalyst, the In-doped catalysts revealed no additional MB absorption band during its degradation, indicating a direct photodegradation (without generation of intermediate products) of the dye (Fig. 8(b)).

From the absorption spectra of the dye solution presented in Fig. 8, it was possible to analyze the degradation kinetics of MB and the intermediates. For that, we deconvoluted the absorption spectra of MB solution after 90 min UV irradiation (Fig. 9), taking into account the main peaks (Marbán *et al.* 2011) of the original spectrum ( $C_0 = 10$  ppm) of MB, as well as the absorption peaks correspond to different intermediary products (Zhang *et al.* 2001).

From the temporal evolution of the absorption bands of MB and the intermediate products (Fig. 10) for the undoped  $\text{SnO}_2$  catalyst, we can see that while the concentration of MB gradually decreases with illumination time, the concentration of the intermediates initially increases and then decreases, indicating a total degradation of MB in longer time. As has been stated earlier, use of In-doped  $\text{SnO}_2$  nanoparticles as photocatalysts favors a total degradation of MB without forming intermediates.

To demonstrate the effect of In concentration on the photocatalytic activity of  $\text{SnO}_2$  nanoparticles, the results of MB degradation by the undoped and all the In-doped  $\text{SnO}_2$  samples are presented in Fig. 11. The concentration of the dye in the reaction solution at any instant (c) was calculated for all the samples considering the integrated intensity of the absorption bands correspond to MB and  $[(\text{MB})_2]$ , i.e., the 663 and 612 nm absorption bands only. As can be seen, the photocatalytic activity is much superior for the In-doped samples. In addition, the catalytic activity of the nanostructures increases with the increase of In concentration.

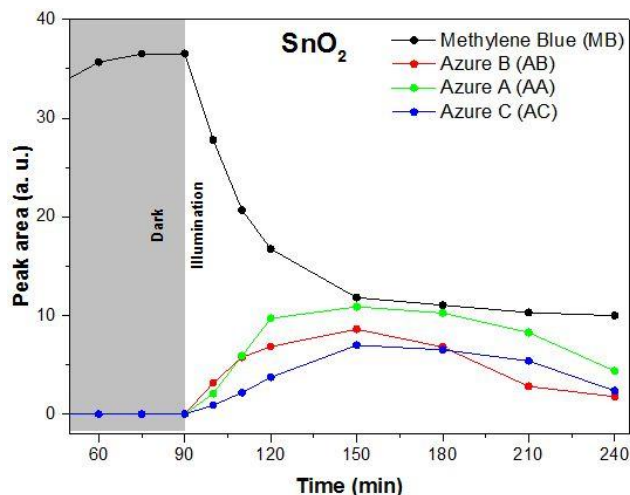


Fig. 10 Temporal degradation of MB and its intermediates over undoped  $\text{SnO}_2$  nanoparticles

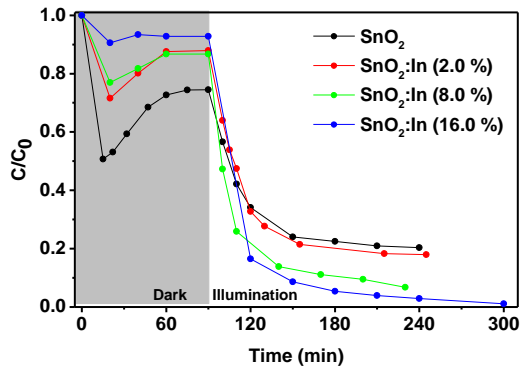


Fig. 11 MB degradation rates of undoped and In-doped  $\text{SnO}_2$  nanoparticles under UV illumination. The concentration ( $C$ ) of MB in the reaction mixture (at a particular time) containing undoped and In-doped  $\text{SnO}_2$  nanoparticles was calculated by considering the intensity of MB and  $[(\text{MB})_2]$  absorption bands at 633 and 612 nm, respectively

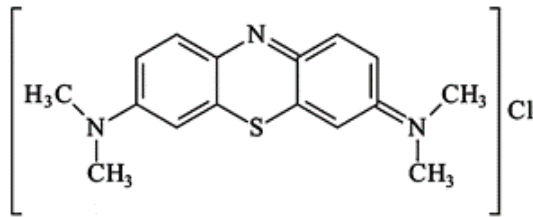
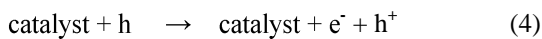
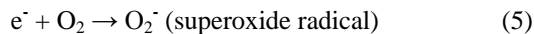


Fig. 12 Molecular structure of MB

When a semiconducting catalyst is illuminated by light with enough energy to generate electron-hole ( $e^-h^+$ ) pairs (Eq. (4))



the photo-generated generated electrons and holes migrate towards the bulk and the catalyst surface. The  $e^-h^+$  pairs that do not recombine again, on the way to the catalyst surface react with available chemical species and the adsorbed MB molecules at the surface of the catalyst. The reactions of photo-generated electrons and holes with oxygen and hydroxyl ions of water produce highly reactive radicals (Eqs. (5) and (6))



To understand the degradation process, we must consider the molecular structure of MB (Fig. 12). As we can see, each MB molecule has four terminal methylene groups ( $-\text{CH}_3$ ). When the reactive radicals ( $\text{O}_2^-$  and  $\text{OH}^*$ ) react with the MB molecule, they attack one by one the bonds between the amino group ( $-\text{N}$ ) and  $-\text{CH}_3$  radical, which we will call as N-demethylation process (where N is the number of  $-\text{CH}_3$  radicals) or degradation of the MB. As has been schematically presents in Fig. 13, the intermediates such as azure B (AB), azure A (AA) and azure C (AC) are produced due to sequential demethylation process of MB.

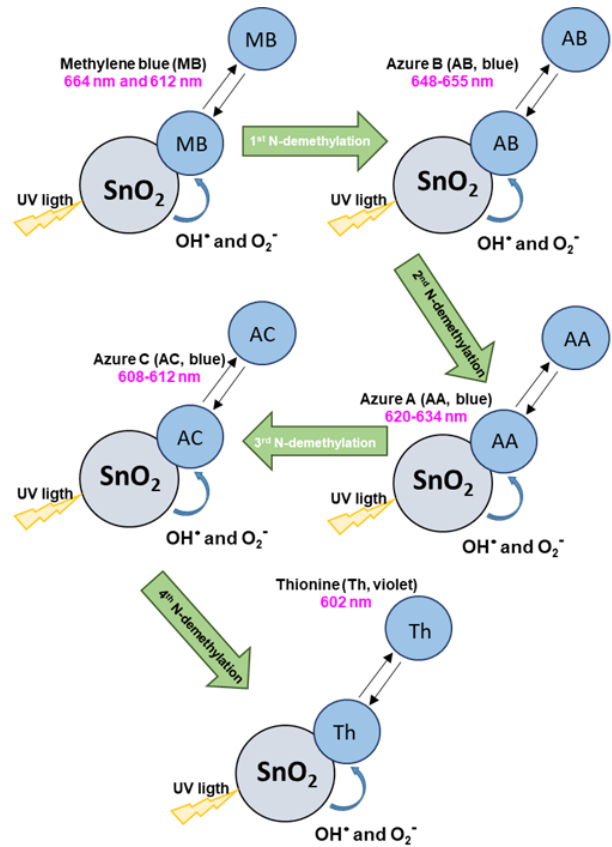


Fig. 13 Schematic representation of possible reaction paths for the N-demethylation of MB in dynamic equilibrium with intermediate at the surface of undoped  $\text{SnO}_2$  nanoparticles under UV illumination

From the normalized degradation curves of the catalysts presented in Fig. 11, it can be clearly seen that the rate of MB photo-degradation by the catalysts improves on In doping. The efficiencies of MB decolorization or the decolorization efficiency (DE) of the catalysts were estimating using Eq. (7) (Mondal *et al.* 2017)

$$DE = \frac{C_0 - C}{C_0} \times 100\% \quad (7)$$

Table 4 Estimated MB removal (adsorption and degradation) efficiencies for undoped and In-doped  $\text{SnO}_2$  catalysts. The adsorbed fraction of MB was calculated from the reduction of MB concentration in the dye solution after 90 min of addition of catalyst under dark (see Fig. 11)

Catalyst	Adsorption percentage	Percentage of photo-degradation	Total dye removal
	[%]	[%]	[%]
$\text{SnO}_2$	25.54	54.10	79.65
$\text{SnO}_2:\text{In}$ (2.0 %)	12.12	69.90	82.02
$\text{SnO}_2:\text{In}$ (8.0 %)	12.27	80.94	93.21
$\text{SnO}_2:\text{In}$ (16.0 %)	7.23	91.66	98.89

where  $C_0$  is the initial concentration of MB and  $C$  is the concentration in the irradiation time. The estimated decolorization efficiency of all the used catalysts are presented in Table 4, considering the total MB removal as the sum of the percentage of MB adsorbed on the surface of the catalyst (in dark) and the percentage degraded in the catalytic process (with illumination). The highest photocatalytic efficiency was observed for the SnO<sub>2</sub> nanoparticles with nominal 16.0 % indium doping.

The kinetics of MB degradation by the catalysts was studied by calculating the reaction rate ( $r$ ) following the Eq. 8, which is a very common expression in Langmuir-Hinshelwood model (L-H) (Mondal *et al.* 2017)

$$r = \frac{dC}{dt} = \frac{k_1 k_2 C}{1 + k_2} \quad (8)$$

where  $k_1$  is the apparent rate constant,  $k_2$  is the adsorption constant, and  $C$  is the reactant concentration. As the used MB solution of initial 10 ppm concentration can be considered as a diluted solution, we can use the first-order simplified kinetic model of L-H, which is often used to treat complex oxidation reactions such as MB degradation, which triggers a series of reactions carried out in several steps producing intermediate species (Ali *et al.* 2011). In the first-order kinetic model of L-H, the reaction rate and concentration variation can be expressed as Eqs. (9) and (10)

$$r = \frac{dC}{dt} = -K_{app} C \quad (9)$$

$$\ln\left(\frac{C}{C_0}\right) = \ln\left(\frac{A_t}{A_0}\right) = -K_{app} t \quad (10)$$

where  $C$  is the concentration of MB at time  $t$ ,  $C_0$  is the concentration at equilibrium after adsorption-desorption process, and  $K_{app}$  is the apparent velocity constant, which can be obtained from the variation of absorption peak intensity of MB (at 663 nm) with time. The ratio of the absorbance  $A_t$  of the MB at time  $t$  and  $A_0$  measured at  $t = 0$  must be equal to the concentration ratio  $C/C_0$  of MB. Therefore, from the plots of  $\ln(C/C_0)$  vs irradiation time (Fig. 14) we can obtain a good linear correlation of the data, obtaining two linear regressions associated with a pseudo-first-order velocity constant,  $K_{app}$  ( $k_1$  and  $k_2$ ) (Mondal *et al.* 2017). The first regression is associated with the degradation of MB to intermediary species, while the second regression is due to the degradation of these intermediate products. As can be observe in Fig. 14, only one linear regression can be obtained for the In-doped SnO<sub>2</sub> catalyst containing 16.0 mol % nominal indium, indicating the degradation of MB occurred directly, possibly without production of intermediates.

The velocity constants estimated for the first-order

Table 5 Values of reaction rate constants estimated for MB degradation by undoped and In-doped SnO<sub>2</sub> nanoparticles

Sample	Reaction rate constant $k_1$ [min <sup>-1</sup> ]	Reaction rate constant $k_2$ [min <sup>-1</sup> ]
SnO <sub>2</sub>	0.0264	0.0019
SnO <sub>2</sub> :In (2.0%)	0.0297	0.0021
SnO <sub>2</sub> :In (8.0%)	0.0604	0.0077
SnO <sub>2</sub> :In (16.0%)	0.0185	-

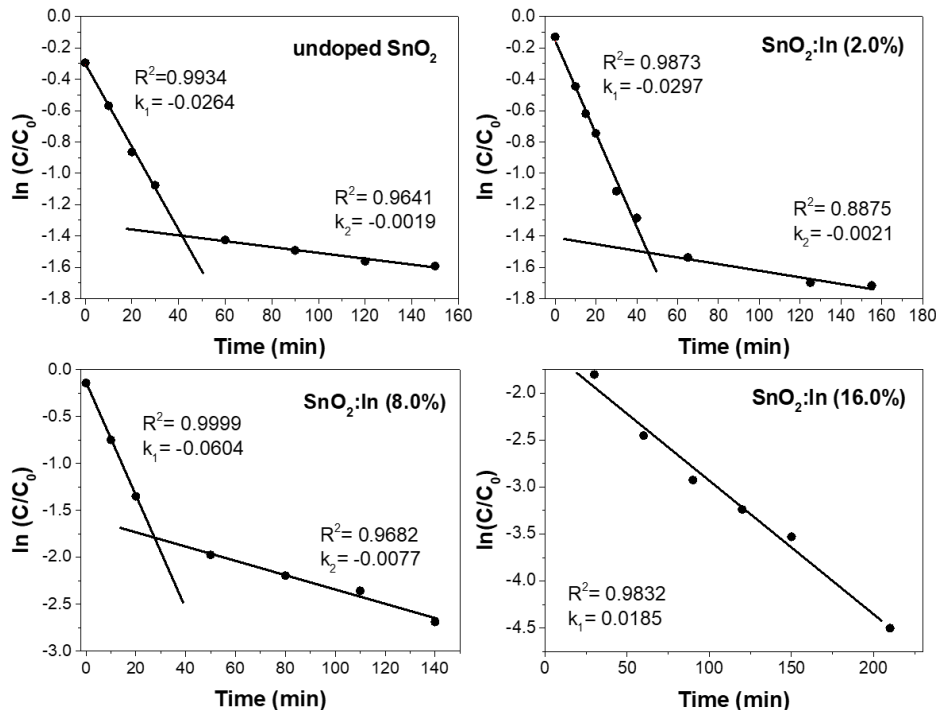


Fig. 14 Kinetics of photodegradation of MB in presence of undoped and In-doped SnO<sub>2</sub> nanoparticles (2.0, 8.0 and 16.0 % nominal)

reaction in the two kinetic regions are presented in Table 5. We can see that the value of  $k_f$  increases with the increase of In concentration in the nanostructures indicating a faster reaction on In incorporation. On the other hand, for the SnO<sub>2</sub> nanoparticles containing a nominal 16.0 mol % of In, while the value of  $k_f$  is a bit smaller (than other samples), the adsorption component is missing or negligible, as has been observed in Fig. 11.

The results presented in the present work clearly demonstrate that In incorporation in small SnO<sub>2</sub> nanoparticles drastically modifies their PL emission behaviors due to an alteration of defect levels in their electronic band structure. Such alterations in defect structures or electronic energy levels severely alter the photocatalytic behaviors of the semiconducting nanostructures.

#### 4. Conclusions

Well-crystalline undoped and In-doped SnO<sub>2</sub> nanoparticles of sub 10 nm sizes could be successfully synthesized through hydrothermal process. While a fraction of incorporated In integrates into the SnO<sub>2</sub> lattice through substitution, the later fraction remains either at interstitial sites or segregate to the surface of the nanoparticles. While the substituting In<sup>3+</sup> ions at Sn<sup>4+</sup> sites create oxygen vacancies to balance the charge neutrality of the crystal lattice, the surface segregated or interstitial In<sup>3+</sup> ions act as electron scavengers or recombination centers. Such behaviors of the incorporated In drastically modify the defect structures of SnO<sub>2</sub> nanoparticles, which not only affects their emission behaviors, but also affects their photocatalytic activity for dye degradation. While the hydrothermally grown small SnO<sub>2</sub> nanoparticles are active photocatalysts for MB degradation under UV illumination, incorporation of In enhances their photocatalytic activity drastically, inducing a full degradation of MB avoiding intermediate steps or production of intermediate by products.

#### Acknowledgments

The authors acknowledge the financial supports extended by VIEP-BUAP, Mexico (grants # VIEP/EXC/2017 and 100236944-BUAP-2018) for the execution of present work.

#### References

Ali, A.M., Emanuelsson, E.A.C. and Patterson, D.A. (2011), "Conventional versus lattice photocatalysed reactions: Implications of the lattice oxygen participation in the liquid phase photocatalytic oxidation with nanostructured ZnO thin films on reaction products and mechanism at both 254 nm and 340 nm", *Appl. Catal. B: Environ.*, **106**, 323-336.

Anuchai, S., Phanichphant, S., Tantraviwat, D., Pluengphon, P., Bovornratanaraks, T. and Inceesungvorn, B. (2018), "Low temperature preparation of oxygen-deficient tin dioxide nanocrystals and a role of oxygen vacancy in photocatalytic

activity improvement", *J. Colloid Interf. Sci.*, **512**, 105-114.

Babu, B., Kadam, A.N., Ravikumar, R.V.S.S.N. and Byon, C. (2017), "Enhanced visible light photocatalytic activity of Cu-doped SnO<sub>2</sub> quantum dots by solution combustion synthesis", *J. Alloys Compd.*, **703**, 330-336.

Bouaine, A., Brihi, N., Schmerber, G., Ulhaq-Bouillet, C., Colis, S. and Dinia, A. (2007), "Structural, Optical, and Magnetic Properties of Co-doped SnO<sub>2</sub> Powders Synthesized by the Coprecipitation Technique", *J. Phys. Chem. C*, **111**(7), 2924-2928.

Busca, G. and Lorenzelli, V. (1982), "Infrared spectroscopic identification of species arising from reactive adsorption of carbon oxides on metal oxide surfaces", *Mater. Chem.*, **7**(1), 89-126.

Carreno, N.L.V., Fajardo, H.V., Maciel, A.P., Valentini, A., Pontes, F.M., Probst, L.F.D., Leite, E.R. and Longo, E. (2004), "Selective synthesis of vinyl ketone over SnO<sub>2</sub> nanoparticle catalysts doped with rare earths", *J. Mol. Catal. A: Chem.*, **207**(1), 91-96.

Chen, H., Ding, L., Sun, W., Jiang, Q., Hu, J. and Li, J. (2015), "Synthesis and characterization of Ni doped SnO<sub>2</sub> microspheres with enhanced visible-light photocatalytic activity", *RSC Adv.*, **5**, 56401-56409.

Cheng, L., Shao, M.-W., Chen, D., Mac, D.D.D. and Lee, S.-T. (2010), "SnO<sub>2</sub> nanowires with strong yellow emission and their application in photoswitches", *Cryst. Eng. Comm.*, **12**, 1536-1539.

Choi, Y.-J., Hwang, I.-S., Park, J.-G., Choi, K.J., Park, J.-H. and Lee, J.-H. (2008), "Novel fabrication of an SnO<sub>2</sub> nanowire gas sensor with high sensitivity", *Nanotechnol.*, **19**(9), 095508.

Diéguez, A., Romano-Rodríguez, A., Vilà, A. and Morante, J.R. (2001), "The complete Raman spectrum of nanometric SnO<sub>2</sub> particles", *J. Appl. Phys.*, **90**, 1550-1557.

Escobedo Morales, A., Sánchez Mora, E. and Pal, U. (2007), "Use of diffuse reflectance spectroscopy for optical characterization of un-supported nanostructures", *Rev. Mex. Fis.*, **S53**(5), 18-22.

Flores, N.M., Pal, U., Galeazzi, R. and Sandoval, A. (2014), "Effects of morphology, surface area, and defect content on the photocatalytic dye degradation performance of ZnO nanostructures", *RSC Adv.*, **4**, 41099-41110.

García-Tecedor, M., Maestre, D., Cremades, A. and Piqueras, J. (2016), "Influence of Cr Doping on the Morphology and Luminescence of SnO<sub>2</sub> Nanostructures", *J. Phys. Chem. C*, **120**(38), 22028-22034.

Gu, F., Wang, S., Cao, H. and Li, C. (2008), "Synthesis and optical properties of SnO<sub>2</sub> nanorods", *Nanotechnol.*, **19**(9), 095708.

Guan, Y., Wang, D., Zhou, X., Sun, P., Wang, H., Ma, J. and Lu, G. (2014), "Hydrothermal preparation and gas sensing properties of Zn-doped SnO<sub>2</sub> hierarchical architectures", *Sens. Actuat. B: Chem.*, **191**, 45-52.

Han, S., Jang, B., Kim, T., Oh, S.M. and Hyeon, T. (2005), "Simple synthesis of hollow tin dioxide microspheres and their application to lithium-ion battery anodes", *Adv. Funct. Mater.*, **15**, 1845-1850.

Higler, R. and Sprake, J. (2017), "Doping colloidal bcc crystals - interstitial solids and meta-stable clusters", *Sci. Rep.*, **7**, 12634.

Horvath, E., Kristof, J., Nasser, H., Frost, R.L., De Basattisti, A. and Redey, A. (2005), "Investigation of SnO<sub>2</sub> thin film evolution by thermoanalytical and spectroscopic methods", *Appl. Surf. Sci.*, **242**, 13-20.

Huang, H., Tan, O.K., Lee, Y.C., Tran, T.D., Tse, M.S. and Yao, X. (2005), "Semiconductor gas sensor based on tin oxide nanorods prepared by plasma-enhanced chemical vapor deposition", *Appl. Phys. Lett.*, **87**, p. 163123.

Jean, S.-T. and Her, Y.-C. (2009), "Synthesis of Sb-additivated SnO<sub>2</sub> nanostructures and dependence of photoluminescence properties on Sb additivation concentration", *J. Appl. Phys.*,

- 105, 024310.
- Ji, Z., Zhao, L., He, Z., Zhou, Q. and Chen, C. (2006), "Transparent p-type conducting indium-doped SnO<sub>2</sub> thin films deposited by spray pyrolysis", *Mater. Lett.*, **60**, 1387-1389.
- Kansal, S.K., Singh, M. and Sud, D. (2007), "Studies on photodegradation of two commercial dyes in aqueous phase using different photocatalysts", *J. Hazard. Mater.*, **141**(3), 581-590.
- Kou, X., Wang, C., Ding, M., Feng, C., Li, X., Ma, J., Zhang, H., Sun, Y. and Lu, G. (2016), "Synthesis of Co-doped SnO<sub>2</sub> nanofibers and their enhanced gas-sensing properties", *Sens. Actuat. B: Chem.*, **236**, 425-432.
- Li, F., Xu, J., Yu, X., Chen, L., Zhu, J., Yang, Z. and Xin, X. (2002), "One-step solid-state reaction synthesis and gas sensing property of tin oxide nanoparticles", *Sens. Actuat. B*, **81**, 165-169.
- Li, W.-T., Zhang, X.-D. and Guo, X. (2017), "Electrospun Ni-doped SnO<sub>2</sub> nanofiber array for selective sensing of NO<sub>2</sub>", *Sens. Actuat. B: Chem.*, **244**, 509-521.
- Liu, L.Z., Wu, X.L., Gao, F., Shen, J.C., Li, T.H. and Chu, P.K. (2011), "Determination of surface oxygen vacancy position in SnO<sub>2</sub> nanocrystals by Raman spectroscopy", *Solid St. Commun.*, **151**(11), 811-814.
- Marbán, G., Vu, T.T. and Valdés-Solís, T. (2011), "A simple visible spectrum deconvolution technique to prevent the artefact induced by the hypsochromic shift from masking the concentration of methylene blue in photodegradation experiments", *Appl. Catal. A: General*, **402**, 218-223.
- Meduri, P., Pendyala, C., Kumar, V., Sumanasekera, G.U. and Sunkara, M.K. (2009), "Hybrid tin oxide nanowires as stable and high capacity anodes for Li-ion batteries", *Nano Lett.*, **9**(2), 612-616.
- Mondal, S., De Anda Reyes Ma, E. and Pal, U. (2017), "Plasmon induced enhanced photocatalytic activity of gold loaded hydroxyapatite nanoparticles for methylene blue degradation under visible light", *RSC Adv.*, **7**, 8633-8645.
- Peche-Herrero, M.A., Maestre, D., Ramírez-Castellanos, J., Cremades, A., Piqueras, J. and González-Calbeta, J.M. (2014), "The controlled transition-metal doping of SnO<sub>2</sub> nanoparticles with tunable luminescence", *Cryst. Eng. Comm.*, **16**, 2969-2976.
- Reddy, C.V., Babu, B. and Shim, J. (2017), "Synthesis of Cr-doped SnO<sub>2</sub> quantum dots and its enhanced photocatalytic activity", *Mater. Sci. Eng. B*, **223**, 131-142.
- Reddy, C.V., Babu, B., Vattikuti, S.V.P., Ravikumar, R.V.S.S.N. and Shim, J. (2016), "Structural and optical properties of vanadium doped SnO<sub>2</sub> nanoparticles with high photocatalytic activities", *J. Lumin.*, **179**, 26-34.
- Sánchez Zeferino, R., Pal, U., Meléndrez, R., Durán-Muñoz, H.A. and Barboza Flores, M. (2013), "Dose enhancing behavior of hydrothermally grown Eu-doped SnO<sub>2</sub> nanoparticles", *J. Appl. Phys.*, **113**, p. 064306.
- Shalan, N.M., Hamad, D., Abdel-Latief, A.Y. and Abdel-Rahim, M.A. (2016), "Preparation of quantum size of tin oxide: Structural and physical characterization", *Prog. Nat. Sci. Mater. Inter.*, **26**(2), 145-151.
- Shang, G., Wu, J., Huang, M., Lin, J., Lan, Z., Huang, Y. and Fan, L. (2012), "Facile Synthesis of Mesoporous Tin Oxide Spheres and Their Applications in Dye-Sensitized Solar Cells", *J. Phys. Chem. C*, **116**(38), 20140-20145.
- Shanmugam, N., Sathya, T., Viruthagiri, G., Kalyanasundaram, C., Gobi, R. and Ragupathy, S. (2016), "Photocatalytic degradation of brilliant green using undoped and Zn doped SnO<sub>2</sub> nanoparticles under sunlight irradiation", *Appl. Surf. Sci.*, **360**, 283-290.
- Shi, W., Song, S. and Zhang, H. (2013), "Hydrothermal synthetic strategies of inorganic semiconducting nanostructures", *Chem. Soc. Rev.*, **42**, 5714-5743.
- Singh, M.K., Mathpa, M.C. and Agarwal, A. (2012), "Optical properties of SnO<sub>2</sub> quantum dots synthesized by laser ablation in liquid", *Chem. Phys. Lett.*, **536**, 87-91.
- Sun, P., Zhou, X., Wang, C., Wang, B., Xu, X. and Lu, G. (2014), "One-step synthesis and gas sensing properties of hierarchical Cd-doped SnO<sub>2</sub> nanostructures", *Sens. Actuat. B: Chem.*, **190**, 32-39.
- Tadeev, A.V., Delabouglise, G. and Labeau, M. (1999), "Sensor properties of Pt doped SnO<sub>2</sub> thin films for detecting CO", *Thin Solid Films*, **337**, 163-165.
- Teresa, O. (2017), "Effect of Double Schottky Barrier in Gallium-Zinc-Oxide Thin Film", *Trans. Electr. Electron. Mater.*, **18**(6), 323-329.
- Tran, V.-H., Ambade, R.B., Ambade, S.B., Lee, S.-H. and Lee, I.-H. (2017), "Low-temperature solution-processed SnO<sub>2</sub> nanoparticles as a cathode buffer layer for inverted organic solar cells", *ACS Appl. Mater. Interfaces*, **9**, 1645-1653.
- Vignesh, K., Hariharan, R., Rajarajan, M. and Suganthi, A. (2013), "Photocatalytic performance of Ag doped SnO<sub>2</sub> nanoparticles modified with curcumin", *Solid State Sci.*, **21**, 91-99.
- Wager, J.F. (2003), "Transparent electronics", *Science*, **300**, 1245.
- Wang, H. and Rogach, A.L. (2014), "Hierarchical SnO<sub>2</sub> Nanostructures: Recent Advances in Design, Synthesis, and Applications", *Chem. Mater.*, **26**(1), 123-133.
- Wang, J.-J., Lv, A.-F., Wang, Y.-Q., Cui, B., Yan, H.-J., Hu, J.-S., Hu, W.-P., Guo, Y.-G. and Wan, L.-J. (2013), "Integrated Prototype Nanodevices via SnO<sub>2</sub> Nanoparticles Decorated SnSe Nanosheets", *Scientific Reports*, **3**, p. 2613.
- Xiang, X., Zu, X.T., Zhu, S., Wang, L.M., Shutthanandan, V., Nachimuthu, P. and Zhang, Y. (2008), "Photoluminescence of SnO<sub>2</sub> nanoparticles embedded in Al<sub>2</sub>O<sub>3</sub>", *J. Phys. D: Appl. Phys.*, **41**, p. 225102.
- Yanes, A.C., Méndez Ramos, J., del-Castillo, J., Velázquez, J.J. and Rodríguez, V.D. (2010), "Size-dependent luminescence of Sm<sup>3+</sup> doped SnO<sub>2</sub> nano-particles dispersed in sol-gel silica glass", *Appl. Phys. B*, **101**(4), 849-854.
- Zhang, T., Oyama, T., Aoshima, A., Hidaka, H., Zhao, J. and Serpone, N. (2001), "Photooxidative N-demethylation of methylene blue in aqueous TiO<sub>2</sub> dispersions under UV irradiation", *J. Photochem. Photobiol. A: Chem.*, **140**, 163-172.
- Zhang, X., Qin, J., Xue, Y., Yu, P., Zhang, B., Wang, L. and Liu, R. (2014), "Effect of aspect ratio and surface defects on the photocatalytic activity of ZnO nanorods", *Sci. Rep.*, **4**, p. 4596.
- Zhou, G., Ni, S., Sun, X., Wang, X., Wang, Q. and He, D. (2011), "Visible photoluminescence of hydrothermal synthesized Sn<sub>1-x</sub>Ni<sub>x</sub>O<sub>2</sub> nanostructures", *J. Mater. Sci: Mater. Electron.*, **22**, 174-178.
- Zuo, J., Xu, C., Liu, X., Wang, C., Wang, C., Hu, Y. and Qian, Y. (1994), "Study of the Raman spectrum of nanometer SnO<sub>2</sub>", *J. Appl. Phys.*, **75**, 1835-1836.

JL